catalysts

MDPI

Article

Replacing Pyridine with Pyrazine in Molecular Cobalt Catalysts: Effects on Electrochemical Properties and Aqueous H_2 Generation

Lars Kohler [1], Andrea M. Potocny [1], Jens Niklas [1], Matthias Zeller [2], Oleg G. Poluektov [1] and Karen L. Mulfort [1,*]

[1] Division of Chemical Sciences and Engineering, Argonne National Laboratory, Lemont, IL 60439, USA; larskohler227@gmail.com (L.K.); ampotocny@anl.gov (A.M.P.); jniklas@anl.gov (J.N.); oleg@anl.gov (O.G.P.)
[2] Department of Chemistry, Purdue University, West Lafayette, IN 47907, USA; zeller4@purdue.edu
* Correspondence: mulfort@anl.gov

Abstract: Four new molecular Co(II)tetrapyridyl complexes were synthesized and evaluated for their activity as catalysts for proton reduction in aqueous environments. The pyridine groups around the macrocycle were substituted for either one or two pyrazine groups. Single crystal X-ray analysis shows that the pyrazine groups have minimal impact on the Co(II)–N bond lengths and molecular geometry in general. X-band EPR spectroscopy confirms the Co(II) oxidation state and the electronic environment of the Co(II) center are only very slightly perturbed by the substitution of pyrazine groups around the macrocycle. The substitution of pyrazine groups has a substantial impact on the observed metal- and ligand-centered reduction potentials as well as the overall H_2 catalytic activity in a multimolecular system using the [Ru(2,2′-bipyridine)$_3$]Cl$_2$ photosensitizer and ascorbic acid as a sacrificial electron donor. The results reveal interesting trends between the H_2 catalytic activity for each catalyst and the driving force for electron transfer between either the reduced photosensitizer to catalyst step or the catalyst to proton reduction step. The work presented here showcases how even the difference of a single atom in a molecular catalyst can have an important impact on activity and suggests a pathway to optimize the photocatalytic activity and stability of molecular systems.

Keywords: photocatalysis; hydrogen; aqueous; cobalt; macrocycle; pyrazine

Citation: Kohler, L.; Potocny, A.M.; Niklas, J.; Zeller, M.; Poluektov, O.G.; Mulfort, K.L. Replacing Pyridine with Pyrazine in Molecular Cobalt Catalysts: Effects on Electrochemical Properties and Aqueous H_2 Generation. *Catalysts* **2021**, *11*, 75. https://doi.org/10.3390/catal11010075

Received: 22 December 2020
Accepted: 31 December 2020
Published: 7 January 2021

1. Introduction

Catalysts that can transform typically inert but sustainable reagents, such as light and water, to generate high-value fuels are absolutely critical to mitigating atmospheric CO_2 accumulation and climate disruption [1–5]. The development of such catalytic systems can be accelerated using molecular complexes, which provide the opportunity to investigate the impact of chemical and electronic structures on catalytic mechanisms and activities with atomic-level resolution [6–10]. Furthermore, molecular catalysts provide the critical ability to investigate in detail the role of both the active center and supporting environment, as well as their interaction. Recent work has demonstrated that the ligand environments of molecular Co(II) catalyst complexes have outstanding impacts on the overall activity and selectivity in several catalytic transformations [11–16]. For catalytic proton reduction, the activity of Co(II) pentadentate catalysts has shown interesting dependence on the location of pyrazine for pyridyl substitution [17] and the sterics of isoquinoline for pyridine substitution [18]. In transformations that are more demanding than proton reduction, such as CO_2 reduction, the addition of amine groups around the periphery of a tetraazine Co(II) macrocycle provides sites to generate an H-bonding network with a solvent and CO_2 [19,20]. These examples, and many others, illustrate how even subtle changes in molecular structure can have a profound impact on catalytic activity [21,22].

Here, we describe the synthesis, characterization, and activity of four new molecular catalysts for photocatalytic proton reduction in an aqueous environment. The structures

of these catalysts are based on the tetra(pyridyl) coordination of a single Co(II) (Figure 1, structures **1**–**4**) and are derived from an open "macrocycle" catalyst that our group recently described which is composed of amine-bridged 2,2′-bipyridine groups (**O-CAT**) [23]. In the current work, either one or two of the pyridine groups of **O-CAT** are replaced with pyrazine groups to generate the novel catalysts **1**–**4** and we find that the pyrazine groups considerably impact the metal- and ligand-centered reduction potentials. The addition of one pyrazine group on the macrocycle furthest from the bridging amine results in a catalyst (**2**) that is more active for aqueous proton reduction than the parent catalyst, while the three remaining pyrazine catalysts show less activity for proton reduction than **O-CAT**. Ultimately, these results point to an interesting correlation between the electron transfer step with the largest thermodynamic driving force and the observed turnovers of H_2.

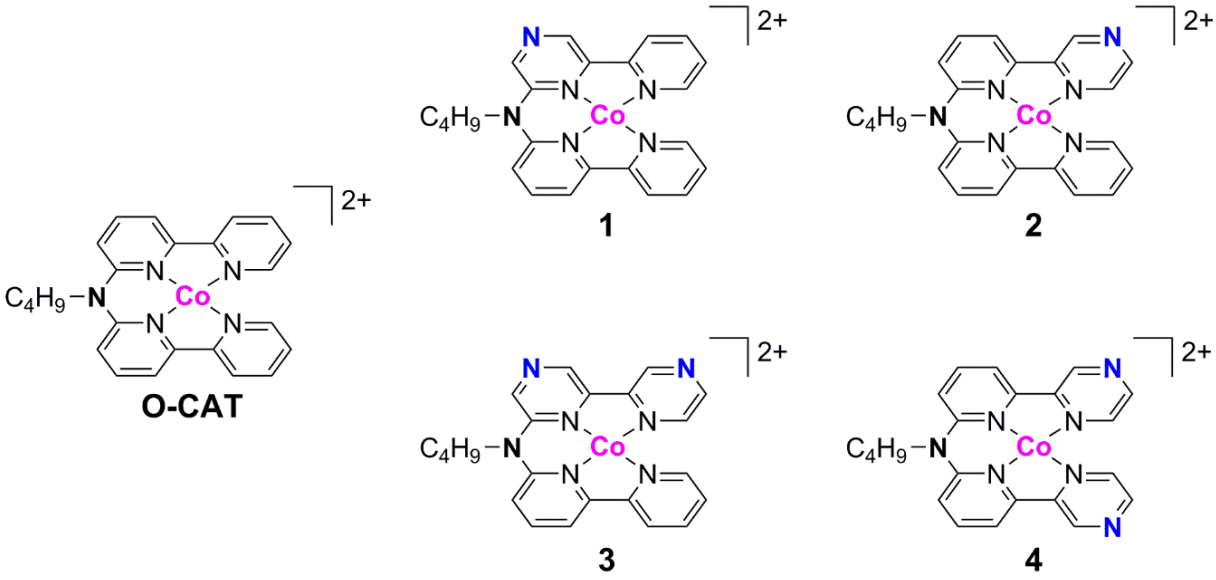

Figure 1. Chemical structures of parent Co(II)tetra(pyridyl) molecular catalyst with amine-bridged 2,2′-bipyridine groups (**O-CAT**), and its pyrazine-functionalized derivatives **1**–**4**.

2. Results

2.1. Catalyst Synthesis

Catalysts **1**–**4** are derived from the structure of the parent molecule **O-CAT** that our group previously found to be highly active and stable for H_2 generation from aqueous solutions [23]. The synthesis of **O-CAT** was achieved by palladium-catalyzed coupling of 6-amino-2,2′-bipyridine with 6-bromo-2,2′-bipyridine followed by metalation using Co(II) salts [24]. The synthesis of **1**–**4** followed a similar strategy of macrocycle formation, followed by metalation with Co(II), although the introduction of pyrazine groups necessitated an additional coupling step to complete the macrocycle. Briefly, macrocycle formation was accomplished by starting with an appropriately substituted halogenated pyridine or pyrazine, followed by two palladium-catalyzed coupling steps using the Buchwald–Hartwig and Stille methods [25]. The order of these carbon–nitrogen and carbon–carbon bond forming steps was dictated by the pyrazine position around the macrocycle. Full synthesis schemes are presented in Appendix A; the complete synthetic procedures and characterization of structure and purity are presented in the Supporting Information.

2.2. X-ray Crystallography

Single crystals of **1**–**4** were grown by slow diffusion of diethyl ether into saturated acetonitrile solutions of each complex. Despite the difference in the pyrazine substitution around the ligand of the catalysts presented here, the molecular structures of **O-CAT**

and **1**–**4** are nearly indistinguishable (Figure 2, Tables S1–S4). Each Co(II) center is penta-coordinated with a distorted square pyramidal geometry. The four Co(II)-chelating nitrogen atoms of pyridine/pyrazine units occupy the equatorial coordination plane with bond lengths typical for Co(II)poly(pyridyl) complexes (1.901–1.961 Å) and a longer bond to CH_3CN in the axial position (2.116–2.144 Å). Additionally, there is a weak interaction (2.4–2.7 Å) between the Co(II) center and an oxygen atom of one of the two perchlorate counter anions. There is no positional disorder observed in the nitrogen of the pyrazine groups. The two pyrazine-decorated bipyridine units of **1**–**4** that compose the Co(II)-chelating ligand are twisted with respect to each other, rendering the macrocycle as severely distorted from planarity, similar to that observed for **O-CAT**. The torsion angle, as defined by the four bipyridine nitrogen atoms, is 16.8° for **1**, **2**, and **3**, and 13.3° for **4**. Complete crystallographic data are presented in the Supporting Information.

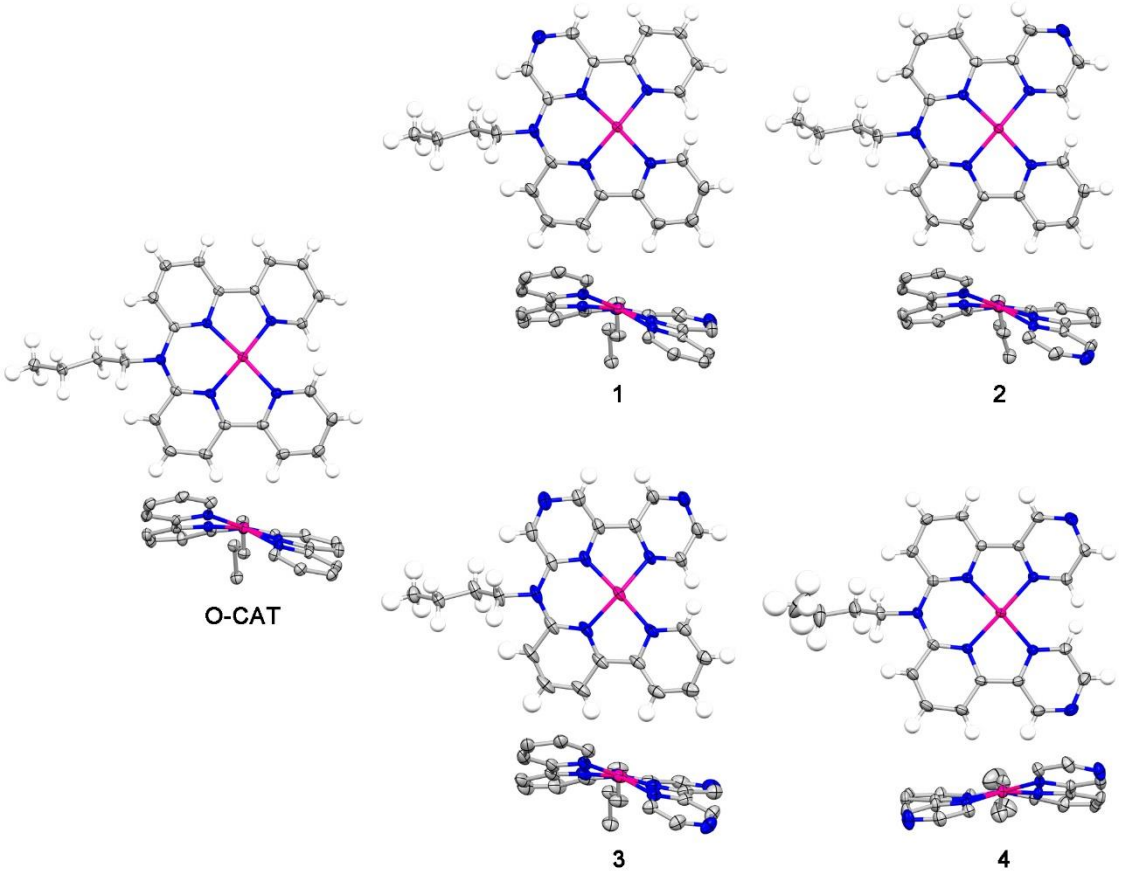

Figure 2. Crystal structures of **O-CAT** and **1**–**4** depicting a view of each macrocycle from the top and from the open end of the complex. Ellipsoids are depicted at 50% probability. Atom labels: carbon, gray; nitrogen, blue; cobalt, magenta. Co(II)-coordinated solvent molecules, disorder, and ClO_4^- counteranions are omitted for clarity. Hydrogen atoms are removed from the end-on view for clarity.

2.3. Electrochemistry

Cyclic voltammetry (CV) was used to investigate how the pyrazine substitution of **1**–**4** impacts the redox properties (Figure 3A, Table 1). The CV scans of **1**–**4** in acetonitrile reveal that the addition of the electron-withdrawing pyrazine groups move the Co(II/I) redox couple to less negative values than for **O-CAT**, which demonstrates that the cobalt center is easier to reduce in the catalysts with pyrazine functionalization. The observed potentials are approximately the same for **1** and **2** (both have one pyrazine group) vs. **3** and **4** (both have two pyrazine groups), which indicates that the number of pyrazine groups is

more important than the specific position of the pyrazine group. For each pyrazine group added to the macrocycle, the Co(II/I) potential shifts anodically by approximately 130 mV, spanning from −0.69 V for **O-CAT** to −0.42 V for complex **3**. A similar trend is observed for the macrocycle (ligand) reduction potentials. Each pyrazine group that is added pushes both the first and second reductions to less negative potentials compared with those of the parent **O-CAT**. Additionally, similar to the trend observed for the metal-centered couples, the ligand reductions of the complexes that contain a single pyrazine group (**1** and **2**) occur at approximately the same potential while the ligand reductions of the complexes that contain two pyrazine groups (**3** and **4**) also occur at very similar potential.

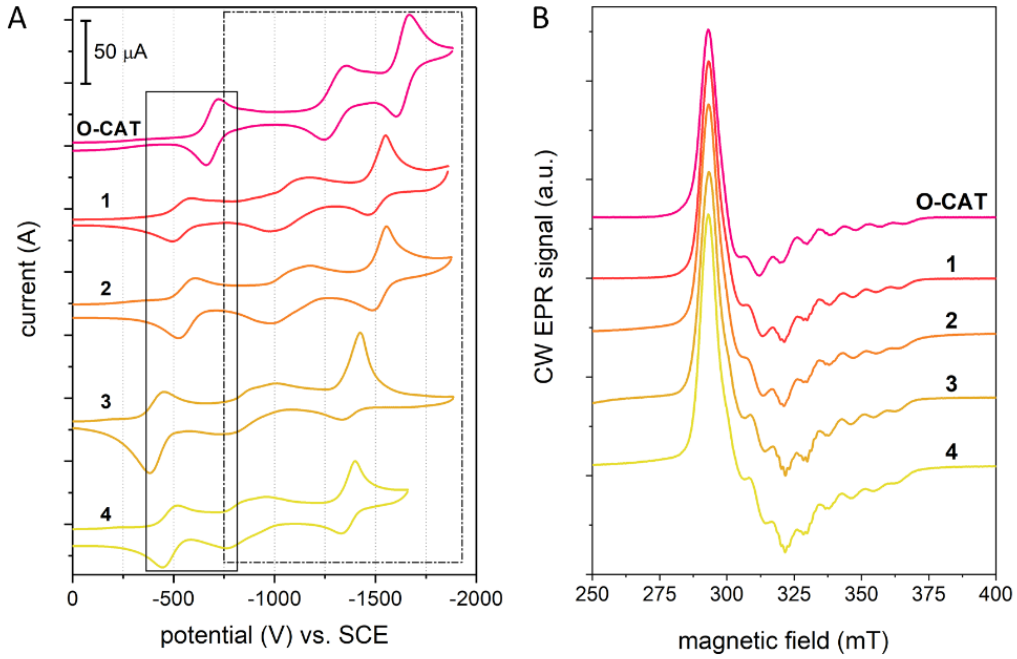

Figure 3. Characterization of the electronic structure of the five Co(II) catalysts. (**A**) Cyclic voltammetry of 1 mM **O-CAT** and **1**–**4** in CH_3CN with 0.1 M $TBAPF_6$ as supporting electrolyte. The solid box highlights the Co(II/I) couple, and the dashed box highlights the ligand reductions. (**B**) Continuous wave X-band EPR spectroscopy of 2 mM **O-CAT** and **1**–**4** in 1:1 CH_3CN:CH_2Cl_2 at 30 K. The simulation of these spectra and magnetic resonance parameters are found in the Supporting Information.

Table 1. Summary of cyclic voltammetry data and H_2 generation activity for **O-CAT** and **1**–**4**.

	$E_{1/2}$ (Co(II/I)) (V vs. SCE) [a]	$E_{1/2}$ ($L^{0/-}$) (V vs. SCE)	$E_{1/2}$ ($L^{-/2-}$) (V vs. SCE)	Initial TOF (H_2/Co/h) [b]	TON at 4 h (H_2/Co)
O-CAT	−0.69	−1.30	−1.64	1017 ± 5	1268
1	−0.54	−1.07	−1.51	450 ± 1	629
2	−0.57	−1.08	−1.52	3419 ± 25	1569
3	−0.42	−0.89	−1.38	376 ± 1	272
4	−0.48	−0.86	−1.37	538 ± 9	324

[a] CV performed in CH_3CN with 0.1 M $TBAPF_6$ as supporting electrolyte; potentials referenced to SCE using ferrocene as internal standard. [b] TOF calculated from linear fit to first 30 min of H_2 production upon illumination.

2.4. Electron Paramagnetic Resonance (EPR) Spectroscopy

Continuous wave (CW) X-band (9.5 GHz) EPR spectroscopy was performed on deaerated frozen solutions of **O-CAT** and **1**–**4** in 1:1 CH_3CN:CH_2Cl_2 to characterize the electronic structure of the cobalt center (Figure 3B). All five spectra are very similar, indicating that the electronic structure of the central Co(II) ion is only very slightly disturbed

by the introduction of one or two pyrazines into the macrocycle. The spectra are typical for mononuclear low-spin Co(II) [23,26–30], which has a d^7 electronic state. The cobalt hyperfine structure (^{59}Co has I = 7/2 with 100% natural abundance) is only resolved in the high-field part of the spectra, resulting in the splitting of the g_z component into eight lines. This splitting, related to hyperfine tensor component A_z, is the largest in **O-CAT**, smaller in **1** and **2** (both with one pyrazine group), and smallest in **3** and **4** (both with two pyrazine groups). The reduced ^{59}Co hyperfine component A_z can be qualitatively interpreted as a consequence of a slight reduction of the electron spin density in the d_{z2} orbital of the Co(II) ion. This trend, observed in the EPR spectra, is in good agreement with the trend of redox potentials of the Co(II/I) redox couple (Figures S28–S32 and Table S5).

The ^{14}N superhyperfine structure is partially resolved and the splitting pattern is consistent with two equivalent nitrogen atoms (^{14}N has I = 1 with >99% natural abundance) in direct contact with the Co(II) ion [29]. This is expected from the nitrogen of two CH_3CN solvent molecules axially coordinating the central Co(II) (for the complete listing of magnetic resonance parameters see Table S5). Note that the superhyperfine interactions of the four nitrogen atoms in the equatorial plane of the cobalt center are not resolved, which is expected for mononuclear Co(II) complexes, since their hyperfine interaction is much smaller than those of axial ligands [31]. Altogether, this confirms that the structure observed in the solid state indeed persists in solution, but now carries an additional two axial CH_3CN ligand molecules.

2.5. H_2 Photocatalysis

The activity of **1**–**4** for aqueous photocatalytic H_2 generation was investigated in a multimolecular system using $[Ru(bpy)_3]^{2+}$ as the molecular photosensitizer and ascorbic acid (AA) as the sacrificial electron donor. We used a set of experimental parameters to evaluate the catalytic activity consistent with the optimal conditions previously described for **O-CAT**. The comparison of the H_2 turnovers (TON) as a function of time under 455 nm LED illumination for each catalyst is presented in Figure 4. We observed that each catalyst immediately began producing H_2 from the aqueous solution following illumination, although the initial turnover frequency (TOF) was different for each catalyst and follows the order **2** > **O-CAT** > **4** > **1** > **3** (see also Table 1). After about four hours of continuous illumination, the TOF had greatly reduced for **2**, **O-CAT**, and **1**, and H_2 production had ceased for **3** and **4**. The only pyrazine-functionalized catalyst that performed better than the parent **O-CAT** was catalyst **2**.

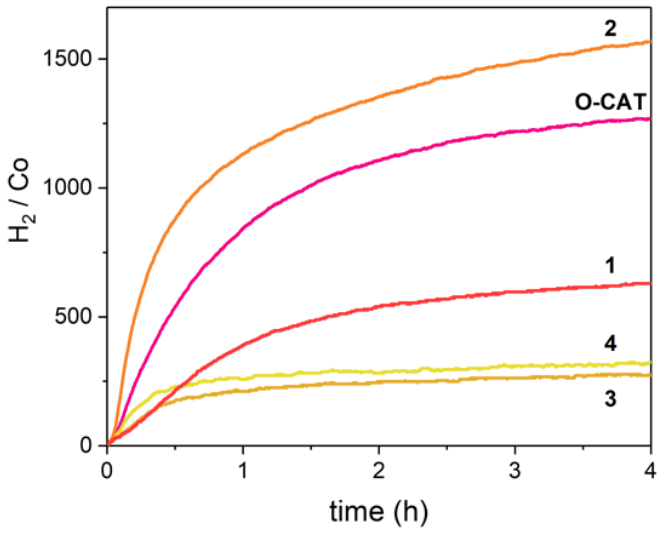

Figure 4. Photocatalytic H_2 generation from water by **O-CAT** and **1**–**4**. Conditions: 5 μM catalyst, 500 μM $[Ru(bpy)_3]Cl_2$, 0.1 M ascorbic acid, pH 4.5, 455 nm LED illumination, 120 mW/cm^2.

3. Discussion

These new pyrazine-functionalized catalysts are based on the basic structure of the previously described **O-CAT** [23]. In this prior work, we demonstrated that **O-CAT** has very high activity for light-activated proton reduction from water when compared with similar Co(II)-based molecular catalysts. Furthermore, analysis of the electrocatalytic activity suggested that the bridging nitrogen between the bipyridine groups can be protonated in the catalyst resting state and that it plays an important role in the mechanism of H_2 generation. Therefore, we proposed that the excellent activity stems from a proton reduction mechanism that proceeds through intramolecular electron and proton transfer steps between the metal center and ligand framework to distribute the two electrons and two proton transfers required to generate H_2 from aqueous protons. This aligns with work from several other groups that have similarly demonstrated that the integration of basic groups into the chemical structure of proton and CO_2 reduction catalysts leads to the ability to bind protons from solution and participate in proton transfer to and from the metal center [22,32].

In agreement with previous work from our group [23] and others on diffusionally governed multimolecular photocatalytic systems [33–35], we propose that the initial steps for photocatalytic H_2 generation are photoexcitation of $[Ru(bpy)_3]Cl_2$ followed by reductive quenching of the excited state by ascorbate (Figure 5A). The reduced photosensitizer, $[Ru(bpy)_2(bpy^{\cdot-})]Cl$, has a reduction potential of −1.52 V vs. SCE [36] and is fully capable of electron transfer to the Co(II) center of catalysts **1**–**4**. Reductive quenching of photoexcited $[Ru(bpy)_3]Cl_2$ by AA^- is thought to be the dominant pathway for photoinduced electron transfer because of the large excess of AA^- even though oxidative quenching by electron transfer also has sufficient driving force to proceed in the absence of other system components [35].

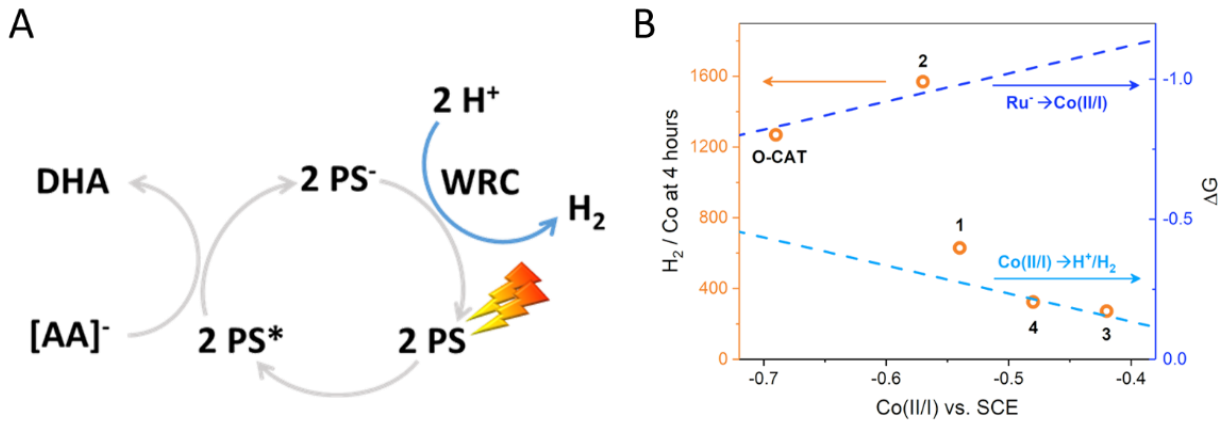

Figure 5. Mechanistic analysis of H_2 photocatalysis by **O-CAT** and **1**–**4**. (**A**) Proposed photocatalytic cycle through reductive quenching of photosensitizer excited state (PS*) by deprotonated ascorbic acid (AA^-). DHA = dehydroascorbic acid; WRC = water reduction catalyst. (**B**) Plot of H_2 turnovers (TON) vs. Co(II/I) reduction potential (left axis) and overlay of ΔG from reduced PS to Co(II) and Co(II/I) to H^+/H_2.

Given the substantial changes to the reduction potentials of **1**–**4** as a function of pyrazine substitution, we had anticipated observing clear correlations between molecular structure, redox potential, and catalytic activity. Contrary to our expectations, when we plot the H_2 TON for **O-CAT** and **1**–**4** versus the Co(II/I) reduction potential, there is no obvious simple relationship (Figure 5B, orange data points). This led us to consider the influence of the catalysts' redox properties on the thermodynamic driving forces for electron transfer between the components of the photocatalytic system. First thinking about the interaction between the reduced photosensitizer and the catalyst, when we plot the difference in free energy (ΔG) for the electron transfer step from $[Ru(bpy)_2(bpy^{\cdot-})]Cl$ to Co(II) (Figure 5B, dark blue dashed line), we observe that **O-CAT** and **2** fall on this line,

but **1**, **3**, and **4** do not. However, if we also consider the overall ΔG for the Co(II/I) potential to the proton reduction potential at pH 4.5, the remaining catalysts **1**, **3**, and **4** do follow this trend (Figure 5B, light blue dashed line). We interpret these relationships as a starting point to understand the complex interplay between molecular structure and electronic properties that contribute to the "dark" steps in the photocatalytic mechanism, which result in the trend we observe in overall activity. For catalysts **O-CAT** and **2**, the driving force for electron transfer from $[Ru(bpy)_2(bpy^{\cdot -})]Cl$ to Co(II) is the smallest among this set of catalysts, so this is likely the rate-limiting step. If this is the case, it would lead to a buildup of dehydroascorbic acid (DHA). Back electron transfer to DHA from $[Ru(bpy)_2(bpy^{\cdot -})]Cl$ is likely not a major factor under these conditions since the overall activity of these catalysts is the highest among those studied here. By contrast, for catalysts **3** and **4**, ΔG for Co(II/I) to the proton reduction potential is the smallest among this set of catalysts, so the steps of the mechanism between the catalyst and the aqueous protons are likely limiting overall activity. If the electron transfer step from the catalyst to protons for **3** and **4** is rate limiting, we are likely to generate a buildup of the Co(I) intermediate, which in general can be a quite labile oxidation state and we presume that these catalysts are not as stable under the conditions investigated here.

The large difference in activity between **1** and **2** cannot be explained by the trends in ΔG since their Co(II/I) redox potentials are nearly identical. However, previous work on a series of Co(II)penta(pyridyl) complexes used for proton reduction found that pyrazine substitution equatorial to the Co(II) center results in much more active catalysts than pyrazine substitution axial to the Co(II) center [17]. We can make similar conclusions with this set of macrocyclic Co(II) catalysts: pyrazine substitution adjacent to the bridging amine (**1**) appears to dramatically impact catalyst stability, possibly as a result of resonance destabilization across the two bonds that separate the pyrazine nitrogen from the tertiary amine.

In this study, the main experimental variable is the molecular structure of the catalyst, specifically the number and location of pyrazine functional groups. However, we recognize that with the different structures and associated variation in both the metal- and ligand-centered redox potentials, there may be different optimal conditions (e.g., pH, light intensity, concentration, photosensitizer ratio, and sacrificial electron donor) for each complex [35,37,38]. Furthermore, the catalyst stability and/or ability to recycle the catalyst may be enhanced by immobilization on a variety of different substrates. It has been demonstrated that immobilizing molecular catalysts onto electrode materials, nanoparticles, graphene, carbon nanotubes, metal–organic frameworks, and even proteins has resulted in hybrid catalyst materials that are more stable and efficient than in homogeneous solution and occasionally in conditions that preclude activity with just the catalyst alone [9,39–44]. Future work with the pyrazine-functionalized catalysts will focus on optimizing conditions for photocatalysis in homogeneous multimolecular systems and evaluating methods to immobilize the molecular catalysts on electro-active substrates.

4. Materials and Methods

4.1. General Methods

^{1}H NMR was performed on a Bruker DMX 500 and referenced to tetramethylsilane (TMS) or residual non-deuterated solvent peaks. Electrospray ionization mass spectrometry (ESI-MS) were collected on a ThermoFisher LCQ Fleet (Waltham, MA, USA) from diluted methanol or acetonitrile solutions in positive ionization mode. Elemental analysis was performed by Midwest Microlab, LLC (Indianapolis, IN, USA). H_2 photocatalysis measurements were performed as previously described [23].

Cyclic voltammetry was conducted using a standard three-electrode cell on a BioAnalytical Systems (BAS, West Lafayette, IN, USA) 100B potentiostat and cell stand with a 3 mm diameter glassy carbon working electrode, a Pt wire auxiliary electrode, and an Ag/AgCl pseudo reference electrode (1.5 mm diameter Ag wire coated with AgCl). Each solution in anhydrous acetonitrile was purged with N_2 prior to measurement and maintained under a

blanket of N_2 during measurement. Tetrabutylammonium hexafluorophosphate (0.1 M) was used as the supporting electrolyte. Ferrocene (purified by sublimation) was added as an internal standard and redox potentials were referenced to the ferrocene–ferrocenium couple (0.40 V vs. saturated calomel electrode (SCE) (acetonitrile) [45]). All scans were performed at 100 mV s^{-1}.

Samples for EPR spectroscopy were prepared as 2 mM solutions of each catalyst in anhydrous 1:1 CH_3CN:CH_2Cl_2 and de-aerated by bubbling with N_2. Solutions were transferred to 4 mm o.d. quartz EPR tubes, sealed under an N_2 atmosphere, and cooled in liquid nitrogen. Continuous wave (CW) X-band (9.5 GHz) EPR experiments were carried out with a Bruker ELEXSYS II E500 EPR spectrometer (Bruker Biospin, Rheinstetten, Germany), equipped with a TE_{102} rectangular EPR resonator (Bruker ER 4102ST). A Helium gas-flow cryostat (ICE Oxford, Witney, UK) and an intelligent temperature controller (ITC) (Oxford Instruments, Abingdon, UK) were used for cryogenic temperatures. Data processing and computer simulations were performed using Xepr (Bruker BioSpin, Rheinstetten) and Easyspin [46] in the Matlab R2018b (The MathWorks, Inc., Natick, MA, USA) environment.

4.2. Synthesis of Complexes **1–4**

Reagents and solvents were obtained from commercial sources and used as received. The synthesis of **O-CAT** was accomplished as previously described [23] and matched all reported characterization. Synthesis schemes can be found in Appendix A and complete synthesis details can be found in the Supporting Information.

4.3. Crystallography

Single crystal X-ray diffraction data for **1–4** were collected at Purdue University. Complete details of data collection and structure solutions can be found in the Supporting Information. The crystal structures of **1–4** have been deposited with the Cambridge Crystallographic Data Centre and can be accessed as structures CCDC 2036712-2036715.

5. Conclusions

In summary, we have described four new Co(II) macrocyclic complexes that are competent photocatalysts for aqueous proton reduction when driven by a molecular photosensitizer and a sacrificial electron donor. Substitution of either one or two pyrazine groups around the macrocycle has dramatic impacts on the redox potentials of both the metal and ligand reductions and important implications for the observed H_2 catalytic activity. Our results suggest that in certain photocatalytic systems, it may be preferable to maximize the ΔG from Co(II/I) to H^+/H_2 rather than the energy difference from the photosensitizer to the catalyst. This is counter to a common goal of developing electrocatalytic systems, where effort is typically focused on trying to minimize the overpotential for proton reduction, which often occurs at, or slightly more negative than, the Co(II/I) couple. In a photocatalytic system, there are more electron transfer steps to consider and systematic structure–activity studies like this one will help provide insight into how to manage competing factors. Ongoing work is focused on identifying and evaluating the catalytic intermediates to further optimize photocatalysis by first-row transition-metal-based molecular complexes.

Supplementary Materials: The following are available online at https://www.mdpi.com/2073-4344/11/1/75/s1, detailed description of synthetic procedures; Figures S1–S27: ^{1}H NMR spectra of synthetic intermediates; details of single crystal X-ray data collection and structural refinement; Tables S1–S4: crystal structure data; Figures S28–S32: simulation of EPR spectra; Table S5: summary of EPR fitting parameters.

Author Contributions: Conceptualization, L.K. and K.L.M.; validation, L.K., A.M.P., J.N., M.Z., O.G.P., and K.L.M.; investigation, L.K., A.M.P., J.N., M.Z., O.G.P., and K.L.M.; resources, J.N., M.Z., O.G.P., and K.L.M.; writing—original draft preparation, K.L.M.; writing—review and editing, L.K., A.M.P., J.N., M.Z., O.G.P., and K.L.M.; visualization, L.K., A.M.P., and K.L.M.; supervision, K.L.M.;

project administration, K.L.M.; funding acquisition, O.G.P. and K.L.M. All authors have read and agreed to the published version of the manuscript.

Funding: The authors gratefully acknowledge support by the U.S. Department of Energy, Office of Science, Office of Basic Energy Sciences, Division of Chemical Sciences, Geosciences, and Biosciences, through Argonne National Laboratory under Contract No. DE-AC02-06CH11357. Funding for the single crystal X-ray diffractometer at Purdue University was made possible through funding by the National Science Foundation through the Major Research Instrumentation Program under Grant No. CHE 1625543.

Institutional Review Board Statement: Not applicable.

Informed Consent Statement: Not applicable.

Data Availability Statement: The data presented in this study are available on request from the corresponding author.

Conflicts of Interest: The authors declare no conflict of interest. The funders had no role in the design of the study; in the collection, analyses, or interpretation of data; in the writing of the manuscript; or in the decision to publish the results.

Appendix A. Synthesis Schemes

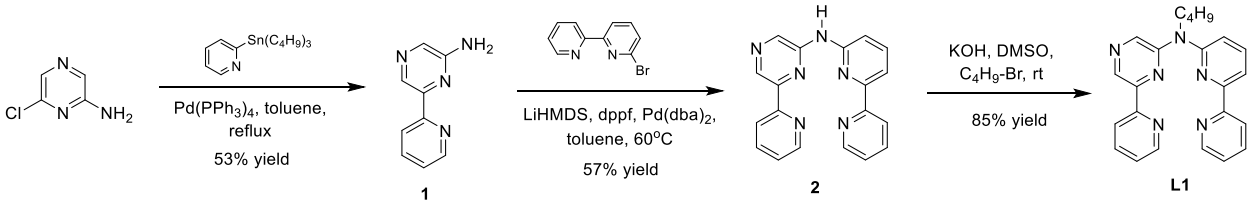

Scheme A1. Synthesis of **L1**.

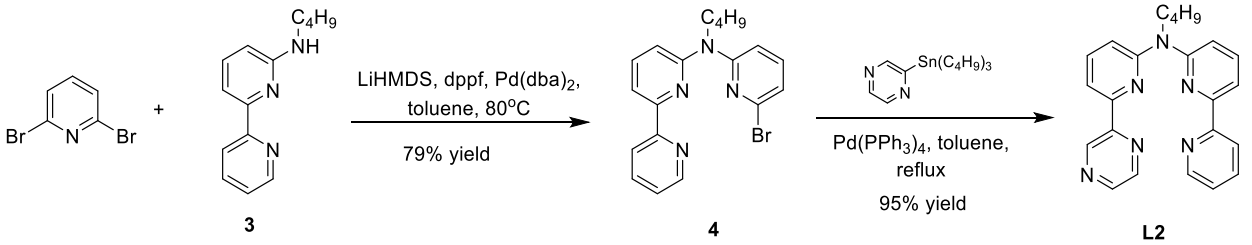

Scheme A2. Synthesis of **L2**.

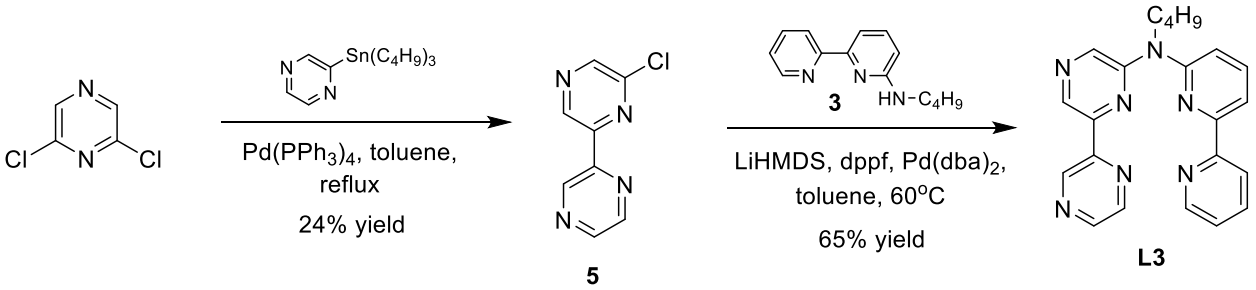

Scheme A3. Synthesis of **L3**.

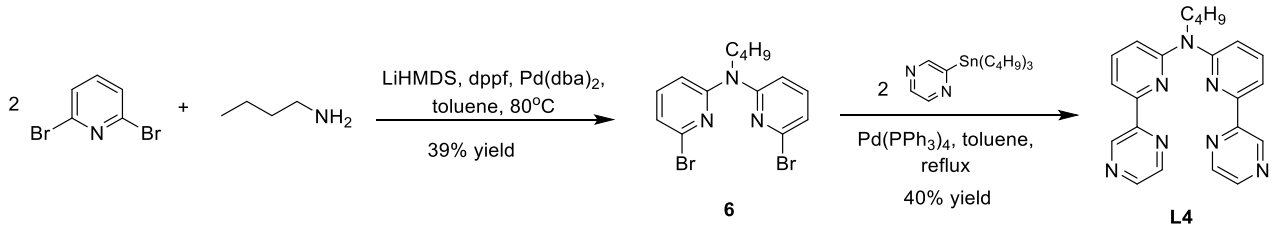

Scheme A4. Synthesis of **L4**.

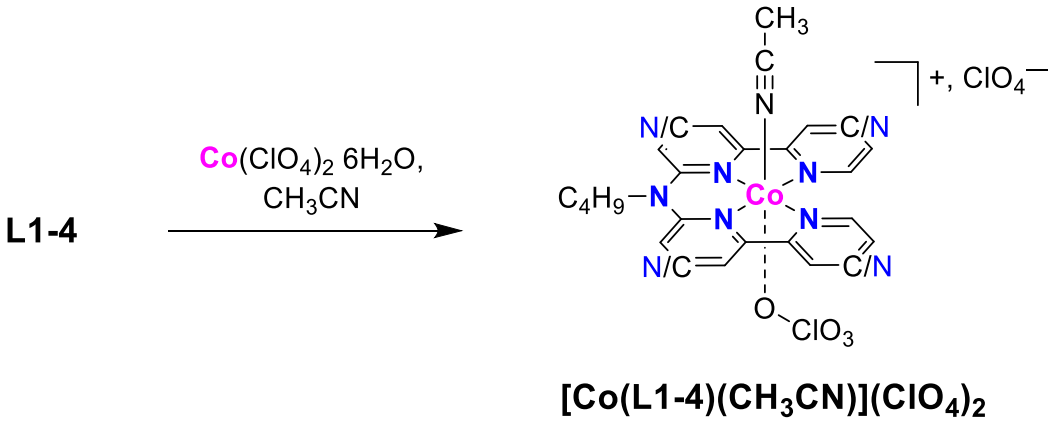

Scheme A5. Synthesis of **1**–**4**.

References

1. Lewis, N.S.; Nocera, D.G. Powering the planet: Chemical challenges in solar energy utilization. *Proc. Natl. Acad. Sci. USA* **2006**, *103*, 15729–15735. [CrossRef] [PubMed]
2. Gust, D.; Moore, T.A.; Moore, A.L. Solar Fuels via Artificial Photosynthesis. *Acc. Chem. Res.* **2009**, *42*, 1890–1898. [CrossRef] [PubMed]
3. Nocera, D.G. Chemistry of Personalized Solar Energy. *Inorg. Chem.* **2009**, *48*, 10001–10017. [CrossRef]
4. Ashford, D.L.; Gish, M.K.; Vannucci, A.K.; Brennaman, M.K.; Templeton, J.L.; Papanikolas, J.M.; Meyer, T.J. Molecular Chromophore–Catalyst Assemblies for Solar Fuel Applications. *Chem. Rev.* **2015**, *115*, 13006–13049. [CrossRef] [PubMed]
5. Matheu, R.; Garrido-Barros, P.; Gil-Sepulcre, M.; Ertem, M.Z.; Sala, X.; Gimbert-Suriñach, C.; Llobet, A. The development of molecular water oxidation catalysts. *Nat. Rev. Chem.* **2019**, *3*, 331–341. [CrossRef]
6. Concepcion, J.J.; House, R.L.; Papanikolas, J.M.; Meyer, T.J. Chemical approaches to artificial photosynthesis. *Proc. Natl. Acad. Sci. USA* **2012**, *109*, 15560–15564. [CrossRef] [PubMed]
7. Eckenhoff, W.T.; Eisenberg, R. Molecular systems for light driven hydrogen production. *Dalton Trans.* **2012**, *41*, 13004–13021. [CrossRef]
8. Berardi, S.; Drouet, S.; Francàs, L.; Gimbert-Suriñach, C.; Guttentag, M.; Richmond, C.; Stoll, T.; Llobet, A. Molecular artificial photosynthesis. *Chem. Soc. Rev.* **2014**, *43*, 7501–7519. [CrossRef]
9. Dalle, K.E.; Warnan, J.; Leung, J.J.; Reuillard, B.; Karmel, I.S.; Reisner, E. Electro- and Solar-Driven Fuel Synthesis with First Row Transition Metal Complexes. *Chem. Rev.* **2019**, *119*, 2752–2875. [CrossRef]
10. Boutin, E.; Merakeb, L.; Ma, B.; Boudy, B.; Wang, M.; Bonin, J.; Anxolabehere-Mallart, E.; Robert, M. Molecular catalysis of CO_2 reduction: Recent advances and perspectives in electrochemical and light-driven processes with selected Fe, Ni and Co aza macrocyclic and polypyridine complexes. *Chem. Soc. Rev.* **2020**, *49*, 5772–5809. [CrossRef]
11. Artero, V.; Chavarot-Kerlidou, M.; Fontecave, M. Splitting Water with Cobalt. *Angew. Chem. Int. Ed.* **2011**, *50*, 7238–7266. [CrossRef] [PubMed]
12. Du, P.; Eisenberg, R. Catalysts made of earth-abundant elements (Co, Ni, Fe) for water splitting: Recent progress and future challenges. *Energy Environ. Sci.* **2012**, *5*, 6012–6021. [CrossRef]
13. Nippe, M.; Khnayzer, R.S.; Panetier, J.A.; Zee, D.Z.; Olaiya, B.S.; Head-Gordon, M.; Chang, C.J.; Castellano, F.N.; Long, J.R. Catalytic proton reduction with transition metal complexes of the redox-active ligand bpy2PYMe. *Chem. Sci.* **2013**, *4*, 3934–3945. [CrossRef]
14. Queyriaux, N.; Jane, R.T.; Massin, J.; Artero, V.; Chavarot-Kerlidou, M. Recent developments in hydrogen evolving molecular cobalt(II)–polypyridyl catalysts. *Coord. Chem. Rev.* **2015**, *304–305*, 3–19. [CrossRef]

15. Hogue, R.W.; Schott, O.; Hanan, G.S.; Brooker, S. A Smorgasbord of 17 Cobalt Complexes Active for Photocatalytic Hydrogen Evolution. *Chem.-Eur. J.* **2018**, *24*, 9820–9832. [CrossRef]
16. Dolui, D.; Khandelwal, S.; Majumder, P.; Dutta, A. The odyssey of cobaloximes for catalytic H_2 production and their recent revival with enzyme-inspired design. *Chem. Commun.* **2020**, *56*, 8166–8181. [CrossRef]
17. Jurss, J.W.; Khnayzer, R.S.; Panetier, J.A.; El Roz, K.A.; Nichols, E.M.; Head-Gordon, M.; Long, J.R.; Castellano, F.N.; Chang, C.J. Bioinspired design of redox-active ligands for multielectron catalysis: Effects of positioning pyrazine reservoirs on cobalt for electro- and photocatalytic generation of hydrogen from water. *Chem. Sci.* **2015**, *6*, 4954–4972. [CrossRef]
18. Wang, P.; Liang, G.; Reddy, M.R.; Long, M.; Driskill, K.; Lyons, C.; Donnadieu, B.; Bollinger, J.C.; Webster, C.E.; Zhao, X. Electronic and Steric Tuning of Catalytic H2 Evolution by Cobalt Complexes with Pentadentate Polypyridyl-Amine Ligands. *J. Am. Chem. Soc.* **2018**, *140*, 9219–9229. [CrossRef]
19. Chapovetsky, A.; Do, T.H.; Haiges, R.; Takase, M.K.; Marinescu, S.C. Proton-Assisted Reduction of CO_2 by Cobalt Aminopyridine Macrocycles. *J. Am. Chem. Soc.* **2016**, *138*, 5765–5768. [CrossRef]
20. Chapovetsky, A.; Welborn, M.; Luna, J.M.; Haiges, R.; Miller, T.F.; Marinescu, S.C. Pendant Hydrogen-Bond Donors in Cobalt Catalysts Independently Enhance CO_2 Reduction. *ACS Cent. Sci.* **2018**, *4*, 397–404. [CrossRef] [PubMed]
21. Khandelwal, S.; Zamader, A.; Nagayach, V.; Dolui, D.; Mir, A.Q.; Dutta, A. Inclusion of Peripheral Basic Groups Activates Dormant Cobalt-Based Molecular Complexes for Catalytic H_2 Evolution in Water. *ACS Catal.* **2019**, *9*, 2334–2344. [CrossRef]
22. Dolui, D.; Ghorai, S.; Dutta, A. Tuning the reactivity of cobalt-based H_2 production electrocatalysts via the incorporation of the peripheral basic functionalities. *Coord. Chem. Rev.* **2020**, *416*, 213335. [CrossRef]
23. Kohler, L.; Niklas, J.; Johnson, R.C.; Zeller, M.; Poluektov, O.G.; Mulfort, K.L. Molecular Cobalt Catalysts for H_2 Generation with Redox Activity and Proton Relays in the Second Coordination Sphere. *Inorg. Chem.* **2019**, *58*, 1697–1709. [CrossRef] [PubMed]
24. Zheng, S.; Reintjens, N.R.M.; Siegler, M.A.; Roubeau, O.; Bouwman, E.; Rudavskyi, A.; Havenith, R.W.A.; Bonnet, S. Stabilization of the Low-Spin State in a Mononuclear Iron(II) Complex and High-Temperature Cooperative Spin Crossover Mediated by Hydrogen Bonding. *Chem.-Eur. J.* **2016**, *22*, 331–339. [CrossRef] [PubMed]
25. Yin, L.; Liebscher, J. Carbon−Carbon Coupling Reactions Catalyzed by Heterogeneous Palladium Catalysts. *Chem. Rev.* **2007**, *107*, 133–173. [CrossRef] [PubMed]
26. Schrauzer, G.N.; Lee, L.P. Cobaloximes(II) and vitamin B12r as oxygen carriers. Evidence for monomeric and dimeric peroxides and superoxides. *J. Am. Chem. Soc.* **1970**, *92*, 1551–1557. [CrossRef] [PubMed]
27. Bakac, A.; Brynildson, M.E.; Espenson, J.H. Characterization of the structure, properties, and reactivity of a cobalt(II) macrocyclic complex. *Inorg. Chem.* **1986**, *25*, 4108–4114. [CrossRef]
28. Baumgarten, M.; Lubitz, W.; Winscom, C.J. EPR and ENDOR studies of cobaloxime(II). *Chem. Phys. Lett.* **1987**, *133*, 102–108. [CrossRef]
29. Niklas, J.; Mardis, K.L.; Rakhimov, R.R.; Mulfort, K.L.; Tiede, D.M.; Poluektov, O.G. The Hydrogen Catalyst Cobaloxime: A Multifrequency EPR and DFT Study of Cobaloxime's Electronic Structure. *J. Phys. Chem. B* **2012**, *116*, 2943–2957. [CrossRef]
30. Mukherjee, A.; Kokhan, O.; Huang, J.; Niklas, J.; Chen, L.X.; Tiede, D.M.; Mulfort, K.L. Detection of a charge-separated catalyst precursor state in a linked photosensitizer-catalyst assembly. *Phys. Chem. Chem. Phys.* **2013**, *15*, 21070–21076. [CrossRef]
31. Wirt, M.D.; Bender, C.J.; Peisach, J. Electron Spin Echo Envelope Modulation (ESEEM) Spectroscopy of Cobalt(II) Bis(dimethylglyoximes): Equatorial Co-N Coupling Parameters. *Inorg. Chem.* **1995**, *34*, 1663–1667. [CrossRef]
32. DuBois, M.R.; DuBois, D.L. The roles of the first and second coordination spheres in the design of molecular catalysts for H2 production and oxidation. *Chem. Soc. Rev.* **2009**, *38*, 62–72. [CrossRef] [PubMed]
33. Khnayzer, R.S.; Thoi, V.S.; Nippe, M.; King, A.E.; Jurss, J.W.; El Roz, K.A.; Long, J.R.; Chang, C.J.; Castellano, F.N. Towards a comprehensive understanding of visible-light photogeneration of hydrogen from water using cobalt(ii) polypyridyl catalysts. *Energy Environ. Sci.* **2014**, *7*, 1477–1488. [CrossRef]
34. Roy, S.; Bacchi, M.; Berggren, G.; Artero, V. A Systematic Comparative Study of Hydrogen-Evolving Molecular Catalysts in Aqueous Solutions. *ChemSusChem* **2015**, *8*, 3632–3638. [CrossRef]
35. Natali, M. Elucidating the Key Role of pH on Light-Driven Hydrogen Evolution by a Molecular Cobalt Catalyst. *ACS Catal.* **2017**, *7*, 1330–1339. [CrossRef]
36. Kalyanasundaram, K. Photophysics, photochemistry and solar energy conversion with tris(bipyridyl)ruthenium(II) and its analogues. *Coord. Chem. Rev.* **1982**, *46*, 159–244. [CrossRef]
37. Losse, S.; Vos, J.G.; Rau, S. Catalytic hydrogen production at cobalt centres. *Coord. Chem. Rev.* **2010**, *254*, 2492–2504. [CrossRef]
38. Pellegrin, Y.; Odobel, F. Sacrificial electron donor reagents for solar fuel production. *Comptes Rendus Chim.* **2017**, *20*, 283–295. [CrossRef]
39. Lee, J.; Farha, O.K.; Roberts, J.; Scheidt, K.A.; Nguyen, S.T.; Hupp, J.T. Metal-organic framework materials as catalysts. *Chem. Soc. Rev.* **2009**, *38*, 1450–1459. [CrossRef]
40. Andreiadis, E.S.; Jacques, P.-A.; Tran, P.D.; Leyris, A.; Chavarot-Kerlidou, M.; Jousselme, B.; Matheron, M.; Pécaut, J.; Palacin, S.; Fontecave, M.; et al. Molecular engineering of a cobalt-based electrocatalytic nanomaterial for H_2 evolution under fully aqueous conditions. *Nat. Chem.* **2013**, *5*, 48–53. [CrossRef]
41. Utschig, L.M.; Soltau, S.R.; Tiede, D.M. Light-driven hydrogen production from Photosystem I-catalyst hybrids. *Curr. Opin. Chem. Biol.* **2015**, *25*, 1–8. [CrossRef] [PubMed]

42. Mulfort, K.L.; Utschig, L.M. Modular Homogeneous Chromophore–Catalyst Assemblies. *Acc. Chem. Res.* **2016**, *49*, 835–843. [CrossRef] [PubMed]
43. Jackson, M.N.; Surendranath, Y. Molecular Control of Heterogeneous Electrocatalysis through Graphite Conjugation. *Acc. Chem. Res.* **2019**, *52*, 3432–3441. [CrossRef] [PubMed]
44. Guiton, B.S.; Stefik, M.; Augustyn, V.; Banerjee, S.; Bardeen, C.J.; Bartlett, B.M.; Li, J.; López-Mejías, V.; MacGillivray, L.R.; Morris, A.; et al. Frontiers in hybrid and interfacial materials chemistry research. *MRS Bull.* **2020**, *45*, 951–964. [CrossRef]
45. Connelly, N.G.; Geiger, W.E. Chemical redox agents for organometallic chemistry. *Chem. Rev.* **1996**, *96*, 877–910. [CrossRef] [PubMed]
46. Stoll, S.; Schweiger, A. EasySpin, a comprehensive software package for spectral simulation and analysis in EPR. *J. Magn. Reson.* **2006**, *178*, 42–55. [CrossRef] [PubMed]